The International Journal of Advanced Manufacturing Technology (2020) 106:4437–4449
https://doi.org/10.1007/s00170-020-04943-5

ORIGINAL ARTICLE

Rotary compression in tool cavity—a new ductile fracture calibration test

Zbigniew Pater[1] · Janusz Tomczak[1] · Tomasz Bulzak[1] · Łukasz Wójcik[1] · Konrad Lis[1]

Received: 30 August 2019 / Accepted: 14 January 2020 / Published online: 20 January 2020

Abstract

Ductile fracture is one of the most common failure modes in hot metal forming. It can be predicted by means of so-called damage functions that describe the relation between stress, deformation and fracture initiation. A practical use of these functions requires the knowledge of the critical damage value of the material that is determined by calibration tests based on compression, tension and torsion. For the prediction to be correct, one must ensure that the modelled and real stresses are in agreement. Previous studies did not offer any effective test for determining critical values of damage under changing load conditions that occur in cross and skew rolling processes, among others. To compensate for this knowledge gap, researchers at the Lublin University of Technology have developed a new test consisting in rotary compression of a test-piece in a cavity between the tools, which is described in this paper. In the proposed test, a cylindrical test-piece is rolled over a cavity (impression) created by grooves on two mating tools. The cavity height is smaller than the test-piece diameter. At the critical value of the forming length, the state of stress induced thereby in the test-piece axis causes fracture. Knowing the critical forming length, it is possible to determine the critical value of damage by numerical modelling. The practical application of the proposed test is illustrated through the case of C45 grade steel subjected to forming in the temperature range 950–1150 °C. The analysis makes use of the normalized Cockcroft-Latham (NCL) criterion of ductile fracture.

Keywords Damage · Rotary compression test · FEM · Experiment

1 Introduction

One of the predominant failure modes in metal forming is ductile fracture which is associated with nucleation, growth and coalescence of voids. In the late 1960s, McClintock [1] and Rice and Tracey [2] demonstrated that ductile fracture is accelerated with an increase in stress triaxiality. According to the results obtained by Johnson and Cook [3], the effect of stress triaxiality on ductile fracture is more significant than that of temperature and strain rate. Several years later, Wierzbicki and Xue [4] showed that besides stress triaxiality, ductile fracture is also affected by the third invariant of the stress deviator.

Over the last several years, researchers have developed a number of fracture models for determining the moment of fracture initiation. These models can be classified as follows [5–8]:

- phenomenological criteria,
- continuum damage mechanics,
- void nucleation, growth and coalescence,
- porosity

Among the above models, phenomenological criteria are considered the easiest to apply in practice. For this reason, they are widely used in commercial software dedicated to analysis of forming processes. The above models are based on the assumption that ductile fracture is associated with an energy change caused by the accumulation of plastic strains leading to fracture, which can be described by the so-called damage criterion. A generalized form of this criterion is expressed as:

$$\int^{\varepsilon_f} \Phi(\sigma) d\varepsilon = C, \tag{1}$$

✉ Zbigniew Pater
z.pater@pollub.pl

[1] Lublin University of Technology, 36 Nadbystrzycka Str, 20-618 Lublin, Poland

where ε_f is the critical plastic strain at fracture, $\Phi(\sigma)$ is the function describing the effect of stress on void nucleation, growth and coalescence and C is the critical value of damage function.

There are many ductile failure criteria which differ with respect to the function $\Phi(\sigma)$. A comparison of these criteria can be found in the specialist literature e.g. in works by Li et al. [9] and Kraisnik et al. [10]. For the present analysis, the highly popular ductile fracture criterion developed by Cockcroft and Latham [11] and modified by Oh et al. [12] was selected, which is expressed as:

$$\int^{\varepsilon_f} \frac{\sigma_1}{\sigma_i} d\varepsilon = C, \tag{2}$$

where σ_i is the equivalent stress and MPa; σ_1 is the maximum principal stress, MPa. The above criterion is often called in the literature as normalized Cockcroft-Latham (NCL) and this name is used throughout this paper.

The practical application of the ductile fracture criterion requires the knowledge of critical damage value, which is determined by means of so-called calibration tests. Currently employed tests are based on compression, tension and torsion, and they involve the use of specimens with shapes amplifying fracture propagation. In sheet forming, calibration tests are predominantly performed by tensile testing of sheet specimens such as dog-bone specimens, notched specimens, flat-grooved specimens and shear specimens [13–16]. The critical damage values are then validated with experimental tests using e.g. the Nakajima test [17–19] or the Erichsen cupping test [20].

In the metal forming of solids, ductile fracture calibration tests are more difficult to perform. It is known that ductile fracture criteria can predict fracture initiation effectively if the modelled and real stresses are in agreement. As a result, compression, tensile and torsional tests are performed on test-pieces of different shapes in order to vary stresses. Compression tests under negative stress triaxialities are performed on cylindrical, ring, flanged and tapered test-pieces [21, 22]. To reduce the impact of friction, Aleksandrov et al. [23] recommend making a recess on the test-piece end and filling it with lubricant. It must be emphasized that if compression tests are performed in hot working conditions, it is difficult to determine fracture initiation. This results from strong thermal radiation of the material, which renders it significantly difficult to capture the initiation and propagation of ductile fracture with a high-speed camera [24]. This problem does not occur in tensile tests where the occurrence of a crack is tantamount to workpiece rupture. Test-pieces used in tensile tests can be smooth round bars or notched round bars [9]. The stress triaxiality obtained in these tests exceeds 0.3 and depends on the notch radius. The least frequently used torsional tests are performed in a two-dimensional state of stress where the stress triaxiality is equal to zero. Test-pieces can be solid [6] or hollow [5]. Sometimes, to change the existing state of stress, additional loads acting on the test-piece in the axial direction are applied [25].

Given the difficulty with determining the critical damage value in hot metalworking conditions, no wonder the number of publications devoted to this problem is scarce. This can particularly be observed with respect to cross and skew rolling processes in which variable stresses occurring in the workpiece axis lead to fracture, a phenomenon which is known as the Mannesmann effect. As shown by Yang et al. [26], in these processes, the material is prone to standard ductile fracture that can be predicted using the fracture criteria described with Eq. (1).

Regarding the use of phenomenological models of ductile fracture in the analysis of cross and skew rolling processes, it must be noted that the first work on this problem was published by Piedrahita et al. in 2005 [27]. These authors used Forge 2005 to determine the effect of basic parameters of cross wedge rolling (CWR) on the damage value calculated by the NCL criterion. In 2009, Wang et al. published the first study showing the distribution of damage on the workpiece surface in the CWR process [28]. The numerical simulation was performed based on the NCL criterion, using Deform 3D. The same criterion was also employed by Silva et al. [29], who used Forge 2008 to investigate the effect of forming angle, temperature and velocity on crack formation in CWR. The propagation of fracture was modelled by the kill element technique. The critical damage value was however determined by tensile testing, which led to differences between the numerical and experimental results. In 2014, Pater and Tofil [30] presented the results of a numerical analysis investigating the tube rolling process in the Diescher mill. Among others, the results showed the NCL ductile fracture in the axial section of the workpiece. Also in 2014, Liu et al. [31] employed the Oh criterion to analyse the relationship between the number of tool passes and the final damage value in CWR. They found that when the process is performed in two stages, it is beneficial to use the highest cross-sectional reduction ratio (approx. 75%) in the first stage. Hai and Hue [32] analysed the CWR process for a railway sleeper screw using the Johnson-Cook fracture criterion. The results of the simulation demonstrated that fracture is caused by low-cycle fatigue of the material. Another solution was proposed by Novella et al. [33], who modified the Oyane-Sato fracture criterion to include the effect of temperature and strain rate. Implemented as a subroutine to Forge 2011, this modified criterion proved to be effective in modelling fracture in the CWR of an AA6082-T6 alloy part formed at 510 °C. The NCL criterion was also used to compare two cases of helical rolling of balls analysed using Simufact.Forming in [34]. The results demonstrated that the highest damage value occurs in the loci where the balls get separated. The NCL criterion of ductile fracture was also investigated with respect to skew rolling performed in a numerically controlled three-roll mill [35]. Using Simufact.Forming,

the authors analysed the rolling process for producing a crankshaft preform. Bulzak et al. [36] determined the distribution of the NCL damage value in ball studs produced by CWR using two tools. The analysis was performed with the use of Deform 3D v.11. Skripalenko et al. [37] used both the same software and ductile fracture criterion to investigate the effect of feed angle on the skew rolling of bars in a two-roll mill. The CWR process for a stepped shaft described in [38] was simulated using Forge NxT1.1. The authors of the study arbitrarily assumed that the loss of material cohesion occurs when the NCL damage is equal to 2.5. As a result, they were able to model the process of cutting end scrap material with end-face cavities. The same approach was adopted in the cross rolling of balls [39] and helical rolling of balls [40]. This time the critical damage value was equal to 3. The analysis of CWR of a drive shaft [41] made use of the critical NCL criterion to predict ductile fracture in C45 steel during tensile testing performed in the temperature range of 900–1200 °C. A comparison of the numerical and experimental results demonstrates that the use of the critical damage values determined by tensile tests in cross rolling processes is incorrect and leads to erroneous conclusions. Therefore, it is necessary to develop a new test for determining critical damage values under varying stress conditions, feasible to perform in hot metalworking conditions. This study proposes a test which consists in performing rotary compression in a cavity between the tools.

2 Principle of the rotary compression test

The term "rotary compression" refers to the type of loading in rotary forming processes such as rotary forging, rotary piercing (Mannesmann process), cross rolling and skew rolling. This type of loading can be induced using two tools (flat, concave or convex) which compress the billet, causing it to rotate at the same time.

Figure 1 shows the schematic design of a rotary compression process that is performed using two flat tools, each tool having a longitudinal tapered cavity. The lower tool is stationary while the upper tool executes plane motion along the cavity. A test-piece of the dimensions $d_0 \times b$ is put inside the lower tool cavity; the test-piece diameter is bigger than the spacing between the cavity bottoms (impression height) which is set equal to $2h$. In its front-end part, the moving tool is notched at an angle γ to ensure that the test-piece is radially compressed and thus cannot be pushed out of the cavity. Along with being deformed the test-piece is rotated by action of the friction forces, which causes it to roll in the tool cavity over a forming length s. The role of the cavity side walls is to prevent axial flow (elongation) of the material. During the forming process, the radial stresses in the test-piece axis oscillate from compressive (the minimum values occur vertically) to tensile (the maximum values are observed in a horizontal direction, reflecting the sliding motion of the upper tool) [42]. The stresses change twice per one revolution of the test-piece. Once the specimen has completed the limit number of revolutions, a fracture is formed in its axial zone. In the proposed test, the main task is to determine the forming length of the lower tool (forming length s) at which cracks begin to occur.

3 Experimental tests

Figure 2 shows the test stand for cross rolling used in experimental tests, available at the Lublin University of Technology. The rolling mill has flat tools with a maximum length of 1000 mm. The speed of the hydraulically-driven moving (upper) tool was maintained constant at 300 mm/s.

Calibration tests were performed on specimens of C45 steel, each test-piece having a diameter of 40 mm and a length of 20 mm. The cavity height was set equal to $2h = 38$ mm. The forming surface of the upper tool was cut at an angle γ of 3.5°. The type of material was selected on purpose, as C45 steel is widely used in machine design and has thoroughly been investigated with respect to workability, which is of vital importance in complex metal forming processes such as cross wedge rolling. Test-pieces were preheated in an electrical chamber furnace to the following temperatures T 950 °C, 1000 °C, 1050 °C, 1100 °C and 1150 °C. After preheating, the test-pieces were put inside the lower tool cavity, its dimensions corresponding to those given in Fig. 1. Set into motion, the upper tool gripped the test-piece and rolled it over the lower tool. An example of the test is shown in Fig. 3. When the forming length s was higher than its critical

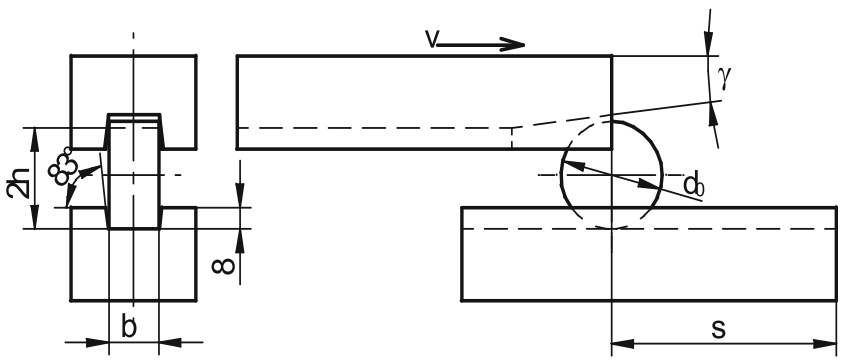

Fig. 1 Schematic design of rotary compression in tool cavity test (dimensions are given in mm)

Fig. 2 Test stand (left) and flat tools (right) used in rotary compression in tool cavity test, where 1—upper tool (moving), 2—lower tool (fixed) and 3—tool cavities in which the test-piece is formed

value, a crack would occur in the axial region, as shown in Fig. 3. In such cases, the forming length s was reduced, and the test was repeated until no crack occurred on the test-piece flank (Fig. 4). After that, the test was repeated two more times, each time at the same parameters; if still no crack could be observed, the applied forming length was considered to be critical for the given billet temperature. It should be mentioned that results of the destructive tests demonstrate that fracture is initiated practically over the entire length of the test-piece axis (Fig. 5). The knowledge of this fact significantly facilitates realization of the proposed test, because then it is enough only to conduct a macroscopic examination of the test-piece flank to determine whether fracture has occurred or not.

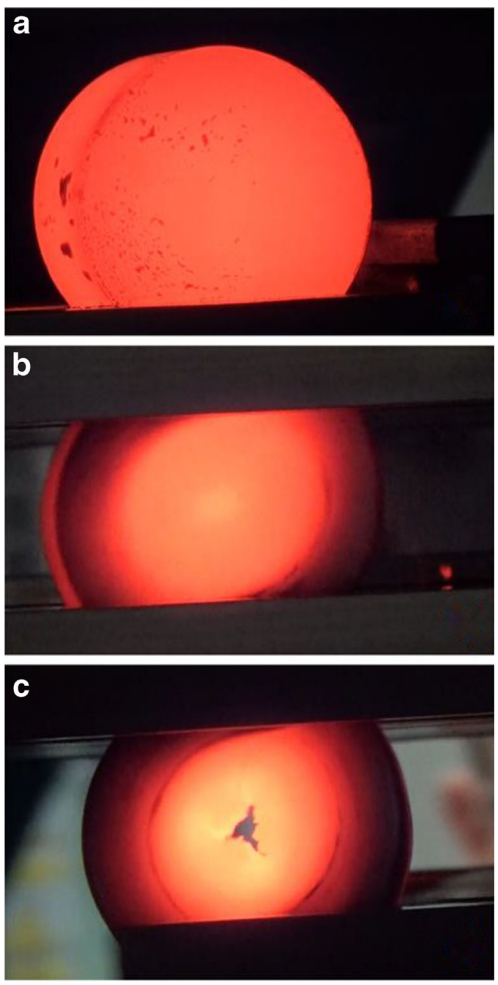

Fig. 3 Rotary compression in tool cavity of a test-piece preheated to 1000 °C and deformed over a length of $s = 275$ mm: **a** test-piece mounting; **b** compression and a visible temperature increase in the test-piece axis; **c** axial crack in the test-piece

The tests also involved measuring the temperature on the test-piece surface. Figure 6 shows the temperature of the test-piece preheated to 1000 °C and rotary compressed over the forming length $s = 230$ mm. The results demonstrate that despite the relatively long forming time, the temperature on the specimen flank, in the axial zone of the test-piece, remains close to the initial temperature of the billet. The layers of the material located on the circumference of the test-piece undergo cooling due to contact with the cold tools. This particular distribution of temperature is desired for the test because the temperature at the locus of fracture remains relatively constant.

The loading force acting on the moving (upper) tool was measured on the test stand. Figure 7 shows the loading force variation in rotary compression performed at $T = 1000$ °C and $s = 230$ mm. An analysis of the loading force variation reveals that the force reaches the highest value at the beginning of the forming process when the test-piece undergoes considerable ovalization. After that, the loading force decreases and remains relatively stable until the end of rotary compression. It is worth emphasizing the fact that the loading force is relatively small in the rotary compression test.

4 FEM analysis

To determine the critical damage value with the proposed rotary compression in cavity test, this process must be numerically modelled by the finite element method. The present analysis is performed with the use of the Simufact.Forming simulation software which was effectively used in previous studies into processes such as cross wedge rolling [43–45], Mannesmann piercing [30, 46, 47], helical rolling of balls [48–50], three-roll skew rolling [35, 51, 52] and other rolling processes [53–57].

Fig. 4 Test-pieces preheated to 1000 °C and deformed over a forming length of **a** 230 mm; **b** 240 mm; **c** 275 mm

For the purpose of the present analysis, a geometric model of the rotary compression process was designed, shown in Fig. 8. The model was identical to the rotary compression test performed under laboratory conditions. The speed of the moving tool was set equal to 300 mm/s, and the GMT material model of C45 steel was described with the following equation:

$$\sigma_{\mathrm{F}} = 2859.85 e^{-0.003125T} \varepsilon^{(0.00004466T-0.10126)} e^{(-0.00002725T+0.0008183)/\varepsilon} \dot{\varepsilon}^{(0.00015115T-0.002748)}, \quad (3)$$

where σ_{F} is the flow stress, MPa; ε is the effective strain, −; $\dot{\varepsilon}$ is the strain rate, s^{-1}; T is the temperature, °C. The GMT model used in the analysis was taken from the Simufact.Forming material database containing material data imported from MatILDa, which is a registered trademark of GMT (Gesellschaft für metallurgische Technologie- und Softwareentwicklung mbH, Berlin).

Friction on the test-piece-tool contact surface was modelled as constant friction described with the following relation:

$$\tau = m\,k, \quad (4)$$

where τ is the shear stress on contact surface, MPa; m is the friction factor (set equal to $m = 0.8$), −; k is the yield stress at pure shear ($k = \sigma_F/\sqrt{3}$), MPa.

The analysis took account of thermal phenomena occurring in the forming process. They depended on the following parameters: test-piece temperature (950 °C, 1000 °C, 1050 °C, 1100 °C, 1150 °C), tool temperature (50 °C), ambient temperature (20 °C), material–tool heat transfer coefficient (10,000 W/m^{2}K) and material–environment heat transfer coefficient (200 W/m^{2}K).

The material was modelled with the use of hexahedral finite elements. The size of a single element was set equal to 1 mm. In total, more than 26,000 finite elements were used to model the test-piece. An automatic remeshing tool was used to reconstruct the mesh at every jump of the strain rate by 0.4. The boundary conditions were defined by the shape of the tools that were modelled as ideally rigid bodies. The implicit finite element solver was used in the calculations.

Figure 9 shows the rotary compression process performed at $T = 1000$ °C and $s = 230$ mm. It can be observed that during the forming process, the test-piece assumes an oval shape characteristic of cross and skew rolling processes. This shape must be maintained in order to induce in the test-piece axis the type of stress that will trigger the Mannesmann effect. To this end, it is necessary to prevent elongation of the test-piece, which can be ensured via action of the side walls of the tool cavity (impression). The circumferential metal flow in the outside layer is accompanied by the displacement of the material in the central region of the test-piece toward its centre, which leads to the formation of funnels on the test-piece flanks. As a result of such metal flow, the test-piece thickness in its axis is reduced (the bigger the reduction, the longer the

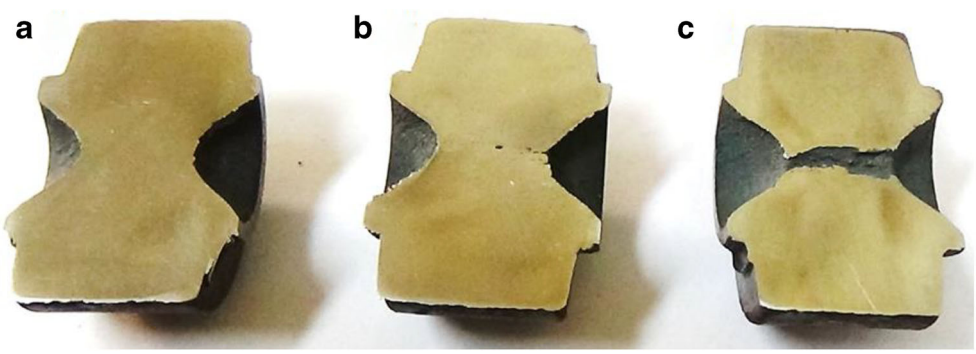

Fig. 5 Cross-sections of the test-pieces deformed at 1150 °C over a forming length of **a** 700 mm; **b** 750 mm; **c** 800 mm

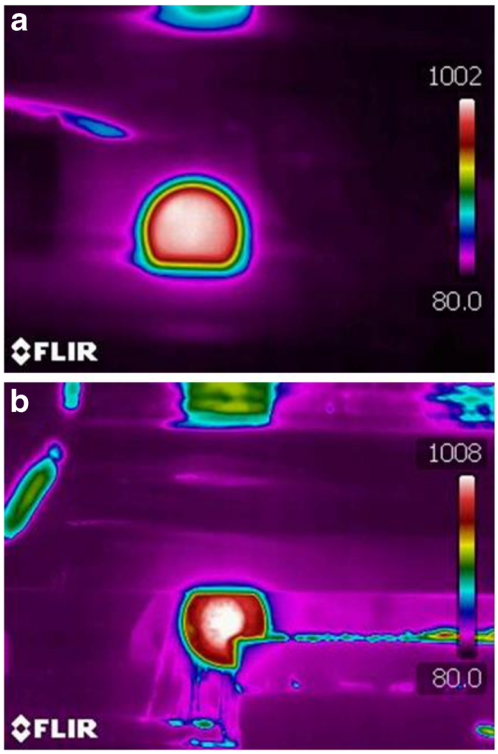

Fig. 6 Temperature on the flank of test-piece during rotary compression in tool cavity, for the forming length $s = 230$ mm: **a** start—the test-piece is mounted in the lower tool cavity; **b** end—the test-piece leaves the lower tool

forming length s), which ultimately leads to the formation of a crack all over the test-piece.

Obtained effective strains of the test-piece preheated to 1000 °C after compression over the forming length $s =$ 230 mm are shown in Fig. 10. The plot reveals that the highest strains occur on the test-piece flanks i.e. in the region where the test-piece is in contact with the working planes of the cavity. In contrast, the strains in the test-piece axis are almost homogenous, which can be considered positive from the point

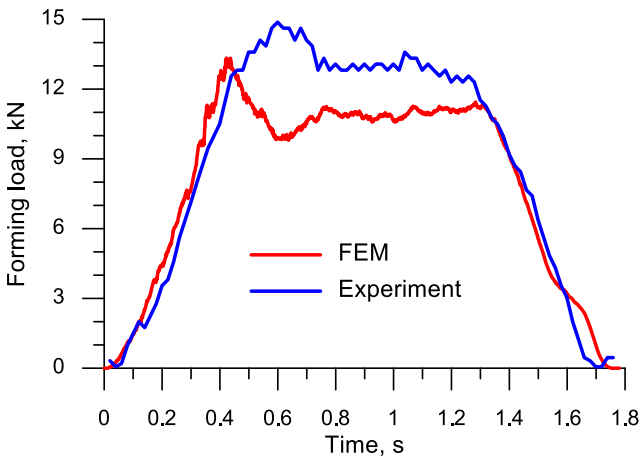

Fig. 7 Variation in the forming load for a test-piece preheated to 1000 °C and rotary compressed over a forming length of $s = 230$ mm

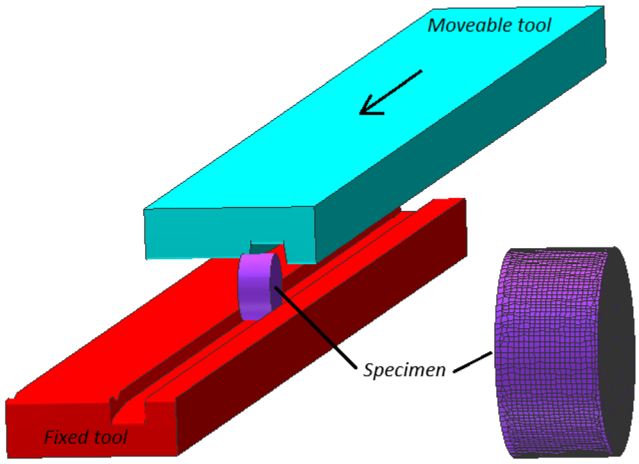

Fig. 8 Geometric model of the rotary compression in tool cavity test, designed in Simufact.Forming

of view of the present analysis. A slight increase in the strains can only be observed on the test-piece end-face.

Figure 11 shows the damage function as calculated by the NCL criterion expressed with Eq. (2). The plot confirms that in the analysed test, fracture will occur in the test-piece axis. The damage function is the highest in the centre of the test-piece, and decreases the closer it is to its end-face.

Interesting observations can be made with respect to temperature distribution in the rotary compressed test-piece. An analysis of the temperature shown in Fig. 12 reveals that due to contact with the tools, the outside layers of the material undergo cooling, and their temperature drops by 100 °C or even more. At the same time, the temperature in the test-piece centre increases, which can be associated with the change of deformation work into heat. The numerical test-piece temperatures agree very well with the experimental findings (Fig. 6). This clearly proves that the temperature slightly increases in the axial zone of the test-piece during rotary compression.

Figure 7 shows the FEM results of the loading force obtained for the analysed case of rotary compression (performed at $T = 1000$ °C and $s = 230$ mm); the figure also shows the experimental loading force. The experimental and numerical loading forces show good qualitative agreement. For the purpose of a quantitative comparison, the loading force results

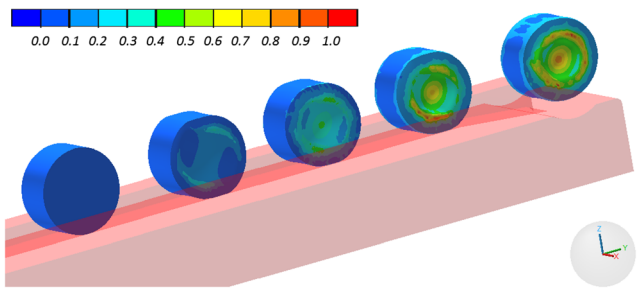

Fig. 9 Test-piece shape progression in rotary compression, conducted at $T = 1000$ °C and $s = 230$ mm, and the damage distribution as measured by NCL criterion (upper tool is hidden for clarity)

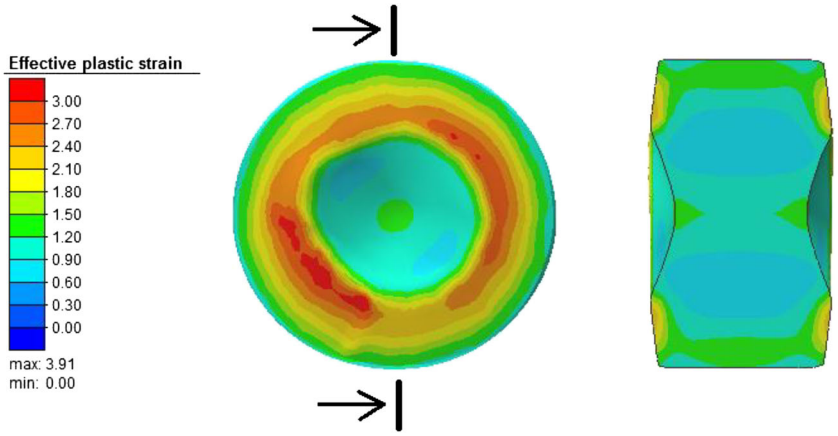

Fig. 10 Effective strain distribution in a test-piece preheated to $T = 1000$ °C and rotary compressed over a forming length 230 mm

were used to determine deformation work for the upper tool velocity set equal to $v = 300$ mm/s. The experimental deformation work was 4.77 kJ, while the numerically calculated deformation work was 4.30 kJ. Hence, the difference between the results is 9.8%. It must be stressed that the experiments involved measuring the loading force on the tool that equalized the deformation force (simulated) and the force associated with overcoming motion resistances generated on the slide guides (not included in the simulation).

Considering the flank temperature and loading force results, one can state that the developed numerical model is a good representation of the real process. Therefore, it can be claimed that the numerical model can be used to determine the critical damage by the rotary compression in tool cavity test.

5 Results and discussion

The experimental tests led to determination of the critical forming length at which fracture takes place. Obtained results are plotted in Fig. 13 and demonstrate that the critical forming length s increases with increasing the temperature. In addition to this, the experimental results demonstrate that at lower forming temperatures cracks propagate rapidly, while in the case of test-pieces preheated to high temperatures, the crack propagation rate is slower.

It should be stressed that the accuracy of the proposed calibration test strongly depends on the accuracy of calculating the critical forming length s. Although the cracking is initiated in the centre of the test-piece, it rapidly propagates into its lateral surfaces. This results from the small thickness of the test-piece, which is additionally reduced due to the formation of cavities on the lateral surfaces. This pattern of crack propagation occurs during a linear displacement of the test-piece over a few millimetres length. Thanks to the research method employed in this study, according to which the fracture initiation was associated with the propagation of cracking into the lateral surface of the test-piece, it was considerably easier to conduct the experimental tests. To increase the accuracy of determining the critical damage, the experimental forming length should be increased only to a very small extent. This, however, will entail more experimental tests and higher research costs.

Knowing the critical forming length s, it was possible to numerically model the rotary compression in cavity test. Calculations were made separately for every tested test-piece temperature, assuming that in every tested case the forming

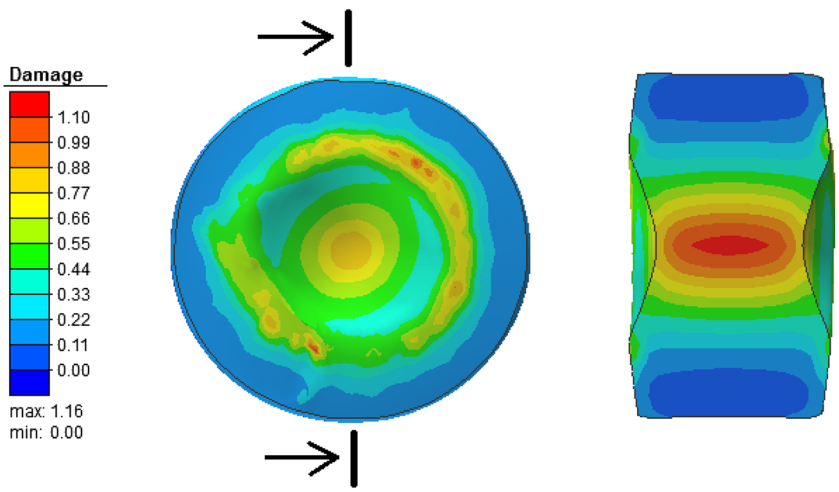

Fig. 11 Damage distribution (as measured by NCL criterion) in a test-piece preheated to $T = 1000$ °C and rotary compressed over a forming length of 230 mm

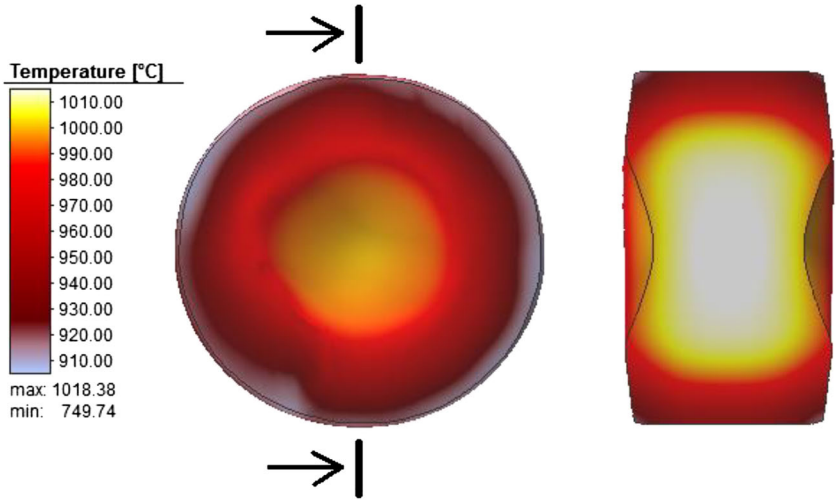

Fig. 12 Temperature (in °C) in a test-piece preheated to T = 1000 °C and rotary compressed over a forming length of 230 mm

process is realized over the critical length s. To give an example, for the test-piece preheated to T = 1000 °C the critical forming length is s = 230 mm (Fig. 13).

For the purpose of quantitative assessment, 11 virtual sensors were located every 2 mm in the test-piece axis to measure individual parameters. Figure 14 shows the effective strain variations calculated with the sensors, the location of which is also marked in this plot. An analysis of the effective strains demonstrates that they increase proportionally in the time range from 0.2 to 1.6 s. In the range 0–0.2 s, the upper tool moves freely, without any contact with the test-piece. On the other hand, for the time t > 1.6 s, the strains do not change, which results from that fact that the test-piece is no longer in contact with its rotation-inducing upper tool. The effective strains in the test-piece axis range 1.1–1.2 approx., achieving higher values at the test-piece surface rather than in its axis.

Interesting observations can be made analysing variations in the principal stress recorded by the virtual sensors for the specific time of rotary compression i.e. t = (0.2–1.6 s), which are plotted in Figs. 15, 16, and 17. The plots reveal the presence of a complex stress state in the test-piece axis – biaxial tension coupled with uniaxial compression inside the test-piece. It can be observed that the further it is from the test-piece end-face, the higher the tensile stresses and the lower the compressive stresses become. At the same time, pure torsion occurs on the end-face in the test-piece axis, which is proved by the fact that the intermediate principal stress determined with sensors 1 and 11 is equal to zero.

As mentioned in the introduction, ductile fracture depends on the stress invariants; it was therefore considered justified to show variation in the stress triaxiality η and the Lode parameter Θ at individual measurement points. The above-mentioned parameters were determined using the following equations:

- stress triaxiality η

$$\eta = \frac{-p}{q} = \frac{\sigma_m}{\sigma_i}, \tag{5}$$

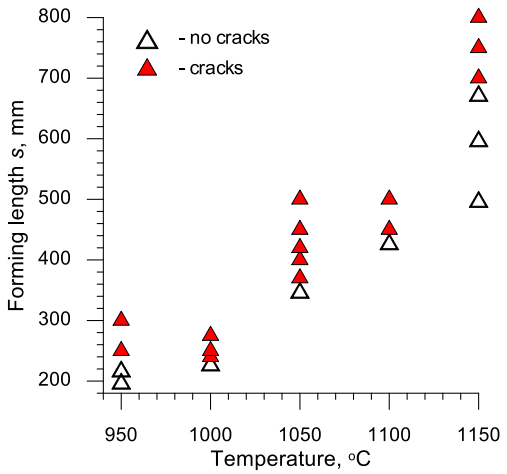

Fig. 13 Plot illustrating the scope of conducted experiments aimed at determining the critical forming length

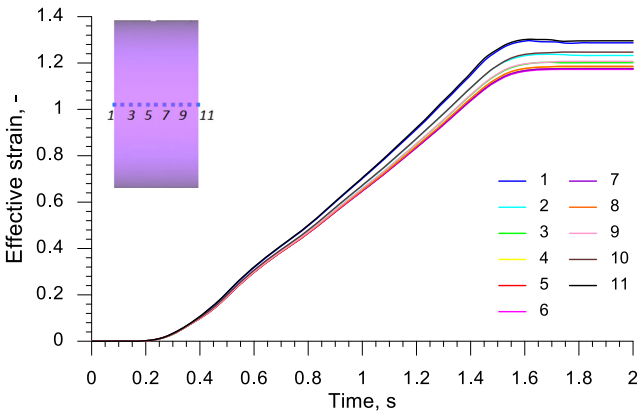

Fig. 14 Effective strain in the test-piece axis versus time, T = 1000 °C

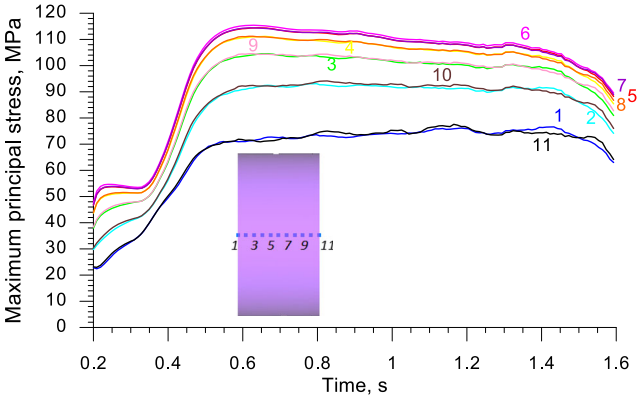

Fig. 15 Distribution of the maximum principal stress σ_1 in the axis of a test-piece preheated to 1000 °C and subjected to rotary compression in tool cavity

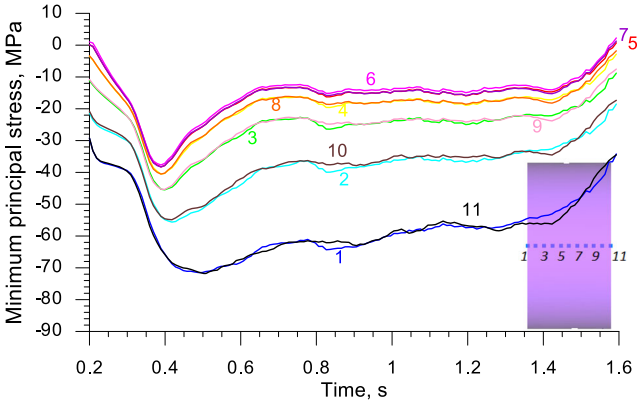

Fig. 17 Distribution of the minimum principal stress σ_3 in the axis of a test-piece preheated to 1000 °C and then subjected to rotary compression in tool cavity

- Lode parameter Θ

$$\theta = 1 - \frac{2}{\pi}\arccos\left[\left(\frac{r}{q}\right)^3\right], \tag{6}$$

where p, q, r denote the stress invariants that are calculated using the equations:

$$p = -\sigma_m = -\frac{1}{3}(\sigma_1 + \sigma_2 + \sigma_3), \tag{7}$$

$$q = \sigma_i = \sqrt{\frac{1}{2}\left[(\sigma_1 - \sigma_2)^2 + (\sigma_2 - \sigma_3)^2 + (\sigma_1 - \sigma_3)^2\right]}, \tag{8}$$

$$r = \left[\frac{27}{2}(\sigma_1 - \sigma_m)(\sigma_2 - \sigma_m)(\sigma_3 - \sigma_m)\right]^{\frac{1}{3}}, \tag{9}$$

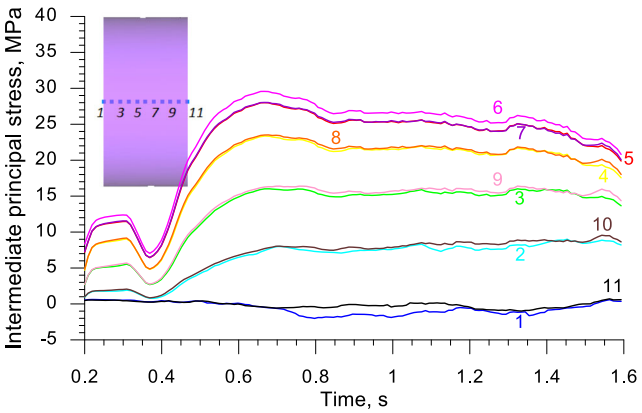

Fig. 16 Distribution of the intermediate principal stress σ_2 in the axis of a test-piece preheated to 1000 °C and then subjected to rotary compression in tool cavity; the stresses measured by virtual sensors 1 and 11 are practically equal to 0, which indicates pure torsion

where σ_1, σ_2, σ_3 are the principal stresses, σ_m is the mean stress and σ_i is the effective stress.

Figure 18 illustrates the stress triaxiality which—depending on the sensor location—ranges from −0.08 to 0.46. The stress triaxiality is higher in the test-piece centre, where its values are close to those obtained by uniaxial tensile testing. An analysis of the Lode parameter variations recorded with individual sensors (Fig. 19) shows that for the principal forming zone, this parameter ranges (−0.4; 0.1). Such values of this parameter point to the presence of strong shear stresses in the test-piece axis. Summing up this part of the analysis, it can be stated that the stresses in the axis of the test-piece subjected to the rotary compression in tool cavity test differ from those occurring in compression, tensile and torsional tests that were previously used for determining critical values of the damage function.

Figure 20 shows the numerically simulated variations in temperature at individual measurement points. The variations demonstrate that the temperature increases during the forming process up to even 20 °C, depending on the sensor location. This increase is caused by the change of deformation work into heat. Due to the fact that the test-piece cool-down

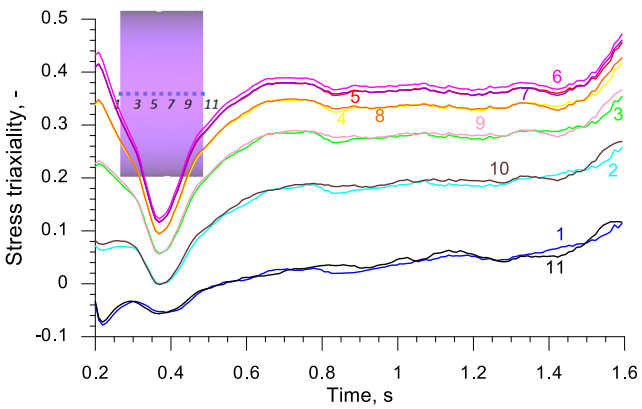

Fig. 18 Stress triaxiality in the axis of a test-piece preheated to 1000 °C

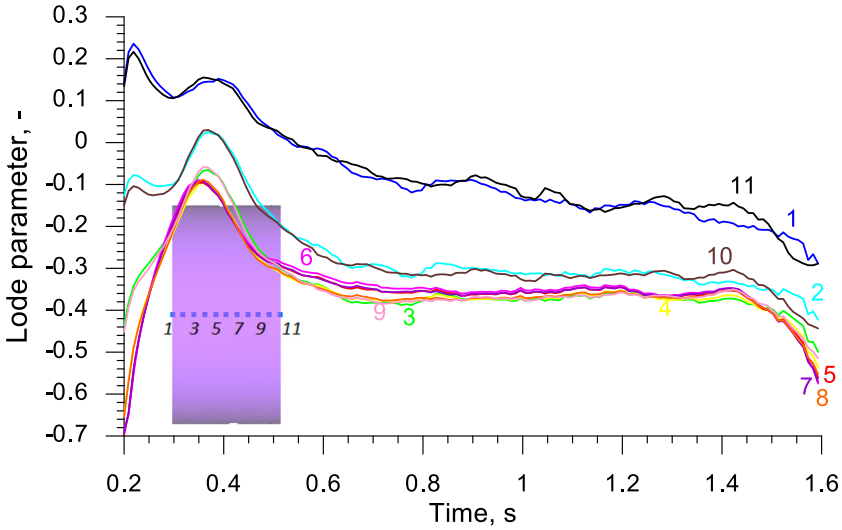

Fig. 19 Variation in the Lode parameter describing the locus of mean principal stress

resulting from its transfer from the furnace to the test stand was omitted in the numerical simulation, the critical damage function was ultimately determined based on the assumption that the temperature in the test-piece axis is equal to the assumed billet temperature.

The increase of the damage function in the test-piece axis (Fig. 21) is similar to the behaviour pattern obtained for the effective strains (Fig. 14). Nevertheless, one can observe bigger differences between the damage function values recorded with the sensors located in the test-piece centre and those positioned on its ends, which results from more intensive tension in the test-piece centre.

To determine the critical damage of the material in a given temperature, the damage function values recorded with individual sensors were averaged. In this way, the plot shown in Fig. 22 was obtained. The data given in this plot clearly indicate that an increase in the billet temperature leads to an increase in the critical value C which—for the tested temperatures—ranges from 0.922 to 3.913.

A flowchart explaining the procedure for determining the critical damage in the rotary compression test is shown in Fig. 23. The determination of the critical damage function (for a given material and a forming temperature T) requires the assumption of the input forming length applied in the rotary compression test. If the fracture occurs in the test-piece, the forming length must be gradually decreased and the calibration test must be repeated until the cracking no longer occurs. If the fracture does not occur in the test-piece during the first test run, the forming length must be increased until the occurrence of cracking. Having the critical forming length s established in this way, it is now necessary to model the rotary compression test numerically in order to determine the mean damage value in the test-piece axis. This value will be equal to the required critical damage value C.

The critical values C calculated by the rotary compression test are much higher and more dependent on the temperature than the critical values determined in the tensile test of notched bars. In accordance with the experimental results presented in [41], the critical NCL damage determined in the tensile test is $C = 0.756 \pm 0.125$ (for C45 steel specimens subjected to tensile testing in the temperature range of 900–1200 °C). By applying the critical damage values established in the rotary

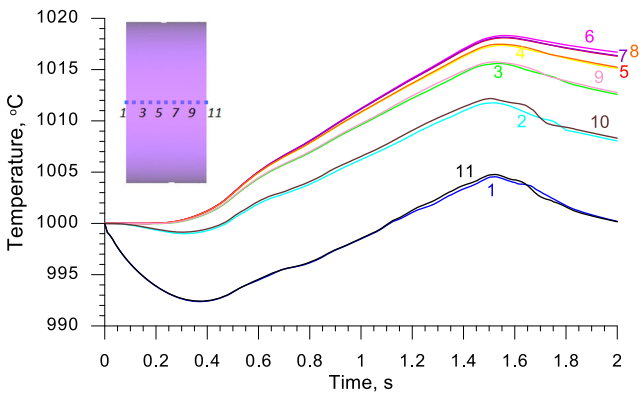

Fig. 20 Temperature in the test-piece axis versus time, $T = 1000$ °C

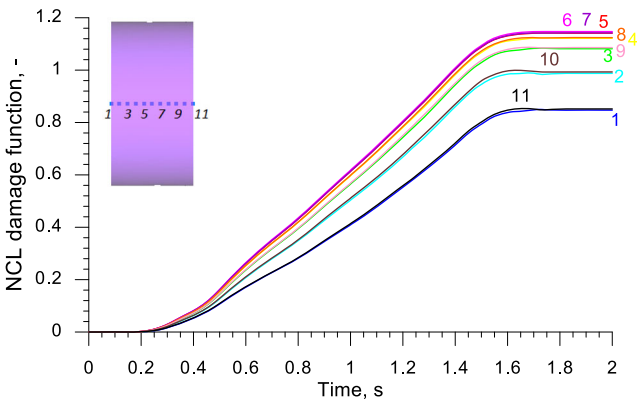

Fig. 21 NCL damage function in the test-piece axis versus time, $T = 1000$ °C

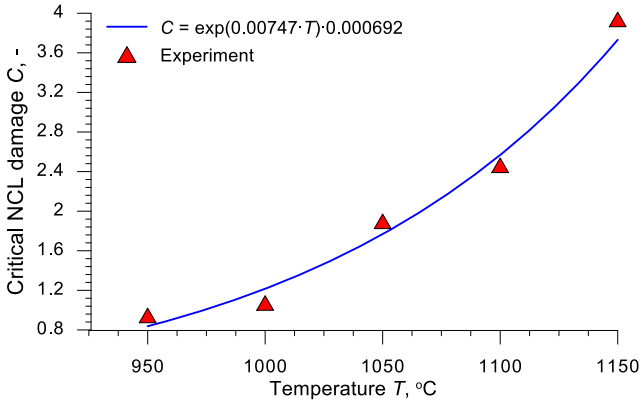

Fig. 22 Relation between critical NCL damage function and temperature determined for C45 steel by rotary compression in tool cavity test

compression test to predict fracture in the CWR case described in [46], one would ensure agreement between the numerical and experimental results.

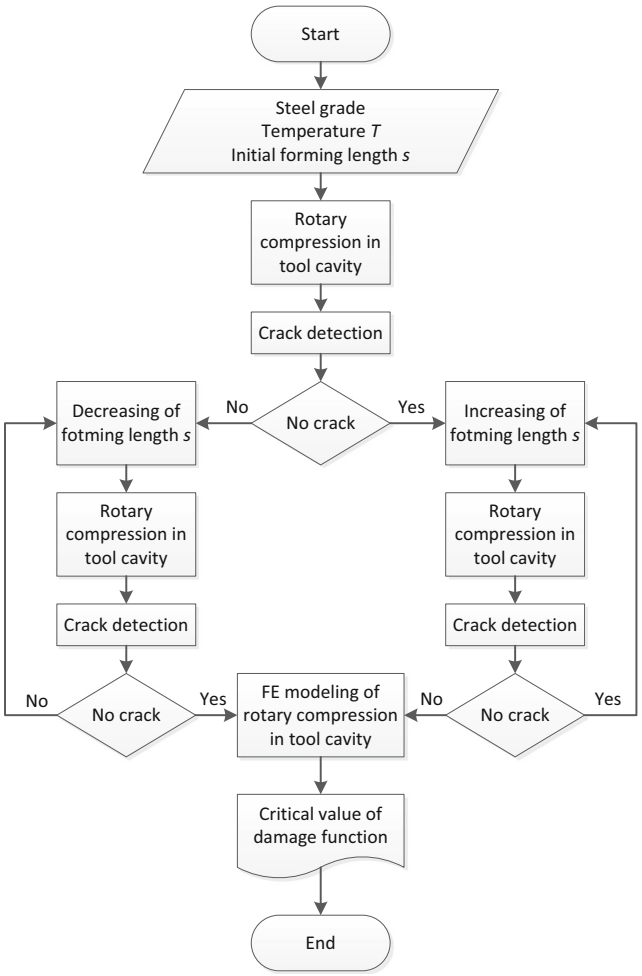

Fig. 23 Flowchart describing the procedure for determining the critical damage value by rotary compression in tool cavity

To facilitate the practical application of obtained results, the critical damage C of C45 steel is described with the following equation dependent on the material temperature T:

$$C = 0.000692 \cdot e^{0.0747\ T}, \tag{10}$$

which is suitable for the temperature range of 950–1150 °C.

6 Conclusions

The following conclusions have been drawn from the study:

- in the proposed rotary compression in tool cavity test, material damage (fracture) occurs in the test-piece axis as a result of the so-called Mannesmann effect;
- despite a relatively long duration of the test (for the forming velocity $v = 300$ mm/s), the temperature in the test-piece axis is similar to that of the billet;
- the state of stress in the test-piece axis is characterized by the presence of maximum and intermediate principal tensile stresses as well as minimum principal compressive stresses, which causes intense shear of the material;
- to determine the critical damage value by means of the proposed rotary compression test, one must know the forming length value at which fracture initiates. In the present analysis, it was the highest forming length value for a given temperature at which no fracture was identified in three repeated tests;
- the critical damage value determined by the rotary compression in tool cavity test strongly depends on the temperature of the material; increasing this temperature leads to an increase in the limit damage value;
- in the hot forming of C45 steel, it is recommended using Eq. (10) that describes the critical damage based on the Cockcroft-Latham ductile fracture criterion.

Funding information The research has been conducted under the project no. 2017/25/B/ST8/00294 financed by the National Science Centre, Poland.

References

1. McClintock FA (1968) A criterion of ductile fracture by growth of holes. J Appl Mech 35:363–371. https://doi.org/10.1115/1.3601204
2. Rice JR, Tracey DM (1969) On the ductile enlargement of voids in triaxial stress fields. J Mech Phys Solids 17:201–217. https://doi.org/10.1016/0022-5096(69)90033-7
3. Johnson GR, Cook WH (1985) Fracture characteristics of three metals subjected to various strains, strain rate and temperatures. Eng Fract Mech 21:31–48. https://doi.org/10.1016/0013-7944(85)90052-9
4. Wierzbicki T, Xue L. On the effect of the third invariant of the stress deviator on ductile fracture. Technical Report 2005;136, Impact and Crashworthiness Laboratory, Massachusetts Institute of Technology
5. Sebek F. Ductile fracture criteria in multiaxial loading – theory, experiments and application. Doctoral Thesis. Brno University of Technology. 2016
6. Coppola T, Cortese L, Folgarait P (2009) The effect of stress invariants on ductile fracture limit in steels. Eng Fract Mech 76:1288–1302. https://doi.org/10.1016/j.engfracmech.2009.02.006
7. Kubik P, Sebek F, Hulka J, Petruska J. Calibration of ductile fracture criteria at negative stress triaxiality. Int J Mech Sci 2016;108–109;90–103. https://doi.org/10.1016/j.ijmecsci.2016.02.001
8. Giglio M, Manes A, Vigano F (2012) Ductile fracture locus of Ti-6Al-4V titanium alloy. Int J Mech Sci 54:121–135. https://doi.org/10.1016/j.ijmecsci.2011.10.003
9. Li H, Fu MW, Lu J, Yang H (2011) Ductile fracture: experiments and computations. Int J Plasticity 27:147–180. https://doi.org/10.1016/j.ijplas.2010.04.001
10. Kraisnik M, Vilotic D, Sidanin L, Stefanovic M (2015) Various approaches to defining the criteria of ductile crack in cold bulk forming processes. Annals of Faculty Engineering Hunedoara - International Journal of Engineering 222:259–267
11. Cockcroft MG, Latham DJ (1968) Ductility and the workability of metals. J I Met 96:33–39
12. Oh SI, Chen CC, Kobayashi S (1979) Ductile fracture in axisymmetric extrusion and drawing. Part II workability in extrusion and drawing. J Eng Ind 101(1):36–44. https://doi.org/10.1115/1.3439471
13. Dunand M, Mohr D (2010) Hybrid experimental-numerical analysis of basic ductile fracture experiments for sheet metals. Int J Solids Struct 47:1130–1143. https://doi.org/10.1016/j.ijsolstr.2009.12.011
14. Quian LY, Fang G, Zeng P, Wang Q (2015) Experimental and numerical investigations into the ductile fracture during the forming of flat rolled 5083-O aluminium alloy sheet. J Mater Process Tech 220:264–275. https://doi.org/10.1016/j.jmatprotec.2015.01.031
15. Gruben O, Hopperstad OS, Borvik T (2013) Simulation of ductile crack propagation in dual-phase steel. Int J Fract 180:1–22. https://doi.org/10.1007/s10704-012-9791-2
16. Mirnia MJ, Shasari M (2017) Numerical prediction of failure in single point incremental forming using a phenomenological ductile fracture criterion. J Mater Process Tech 244:14–43. https://doi.org/10.1016/j.jmatprotec.2017.01.029
17. Bjorklund O, Larsson R, Nilsson L (2013) Failure of high strength steel sheets: experiments and modelling. J Mater Process Tech 213:1103–1117. https://doi.org/10.1016/j.jmatprotec.2013.01.027
18. Bariani PF, Bruschi S, Ghiotti A (2012) Advances in predicting damage evolution and fracture occurrence in metal forming operations. J Manuf Process 14:495–500. https://doi.org/10.1016/j.jmapro.2012.09.013
19. Dizaji SA, Darendeliler H, Kaftanoglu B (2018) Prediction of forming limit curve at fracture for sheet metal using new ductile fracture criterion. Eur J Mech A-Solid 69:255–265. https://doi.org/10.1016/j.euromechsol.2018.01.003
20. Kim SA, Lee YS (2014) Comparative study on failure prediction in warm forming process of Mg alloy sheet by the FEM and ductile fracture criteria. Metall Mater Trans B Process Metall Mater Process Sci 45:445–453. https://doi.org/10.1007/s11663-013-9886-9
21. Gouveia BPPA, Rodrigues JMC, Martins PAF. Ductile fracture in metalworking: experimental and theoretical research. J Mater Process Techn 2000;101;52–63. https://doi.org/10.1016/S0924-0136(99)00449-5
22. Landre J, Pertence A, Cetlin PR, Rodrigues JMC, Martins PAF (2003) On the utilisation of ductile fracture criteria in cold forging. Finite Elem Anal Des 39:175–186. https://doi.org/10.1016/S0168-874X(02)00065-3
23. Alexandrov S, Vilotic D, Konjovic Z, Vilotic M (2013) An improved experimental method for determining the workability diagram. Exp Mech 53:699–711. https://doi.org/10.1007/s11340-012-9676-3
24. Zhu Y, Zeng W, Zhang F, Zhao Y, Zhang X, Wang K (2012) A new methodology for prediction of fracture initiation in hot compression of Ti40 titanium alloy. Mater Sci Eng A 553:112–118. https://doi.org/10.1016/j.msea.2012.05.100
25. Komischke T, Hora P, Domani G, Plamondon M, Kaufmann R (2018) Prediction of crack induced failure phenomena in rolling operations. Procedia Manufacturing 15:176–184. https://doi.org/10.1016/j.promfg.2018.07.192
26. Yang H, Zhang L, Hu Z (1650-1653) The analysis of the stress and strain in skew rolling. Adv Mater Res 2012:538–541
27. Piedrahita F, Garcia Arana L, Chastel Y. Three dimensional numerical simulation of cross-wedge rolling of bars, Proceedings of the 8th International Conference on Technology of Plasticity ICTP, Verona 2005;1–6
28. Wang M, Li X, Du F. Analysis of metal forming in two-roll cross wedge rolling process using finite element method. J Iron Steel Res Int 2009;16(1);38–43. https://doi.org/10.1016/S1006-706X(09)60008-X
29. Silva MLN, Pires GH, Button ST (2011) Damage evolution during cross wedge rolling of steel DIN 38MnSiVS5. Procedia Engineering 10:752–757. https://doi.org/10.1016/j.proeng.2011.04.125
30. Pater Z, Tofil A (2014) FEM simulation of the tube rolling process in Diesche's mill. Adv Sci Technol Res J 8:51–55. https://doi.org/10.12913/22998624.1105165
31. Liu G, Zhong Z, Shen Z (2014) Influence of reduction distribution on internal defects during cross wedge-rolling process. Procedia Engineering 81:263–267. https://doi.org/10.1016/j.proeng.2014.09.161
32. Hai DV, Hue DTH (2015) Finite element simulation and experimental study on internal fracture of railway sleeper screw during cross wedge rolling process. Mater Sci Forum 804:311–314. https://doi.org/10.4028/www.scientific.net/MSF.804.311
33. Novella MF, Ghiotti A, Bruschi S, Bariani PF (2015) Ductile damage modeling at elevated temperature applied to the cross wedge rolling of AA6082-T6 bars. J Mater Process Tech 222:259–267. https://doi.org/10.1016/j.jmatprotec.2015.01.030
34. Pater Z (2016) Numerical analysis of helical rolling processes for producing steel balls. Int J Materials and Product Technology 53(2):137–153. https://doi.org/10.1504/IJMPT.2016.076417
35. Lis K, Wójcik Ł, Pater Z (2016) Numerical analysis of a skew rolling process for producing a crankshaft preform. Open Eng 6:581–584. https://doi.org/10.1515/eng-2016-0087
36. Bulzak T, Pater Z, Tomczak J (2017) Numerical and experimental analysis of a cross wedge rolling process for producing ball studs. Arch Civ Mech Eng 17:729–737. https://doi.org/10.1016/j.acme.2017.02.002
37. Skripalenko MM, Romantsev BA, Galkin SP, Skripalenko MN, Kaputkina LM, Huy TB (2018) Prediction of the fracture of metal

in the process of screw rolling in a two-roll mill. Metallurgist 61(11–12):925–933. https://doi.org/10.1007/s11015-018-0588-z
38. Pater Z, Tomczak J, Bulzak T (2017) FEM simulation of the cross-wedge rolling process for a stepped shaft. Strength Mater 49(4): 521–527. https://doi.org/10.1007/s11223-017-9895-z
39. Pater Z, Tomczak J, Bulzak T (2018) An innovative method for forming balls by cross rolling. Materials 11:1793. https://doi.org/10.3390/ma11101793
40. Pater Z, Tomczak J, Bartnicki J, Bulzak T (2018) Thermomechanical analysis of a helical-wedge rolling process for producing balls. Materials 8:862. https://doi.org/10.3390/met8110862
41. Pater Z, Tomczak J, Bulzak T, Zniszczyński A (2018) The problem of material fracture prediction in cross rolling processes. Adv Sci Technol Res J 12(4):184–189. https://doi.org/10.12913/22998624/100398
42. Pater Z, Walczuk P, Lis K, Wójcik Ł (2018) Preliminary analysis of a rotary compression test. Adv Sci Technol Res J 12(2):77–82. https://doi.org/10.12913/22998624/86812
43. Huang H, Chen X, Fan B, Jin Y, Shu X (2015) Initial billet temperature influence and location investigation on tool wear in cross wedge rolling. Int J Adv Manuf Tech 79:1545–1556. https://doi.org/10.1007/s00170-015-6882-z
44. Tofil A, Tomczak J, Bulzak T (2015) Numerical and experimental study on producing aluminum alloy 6061 shafts by cross wedge rolling using a universal rolling mill. Arch Metall Mater 60(2): 801–807. https://doi.org/10.1515/amm-2015-0210
45. Pater Z, Tomczak J, Bulzak T (2016) Cross-wedge rolling of driving shaft from titanium alloy Ti6Al4V. Key Eng Mat 687:125–132. https://doi.org/10.4028/www.scientific.net/KEM.687.125
46. Lu L, Wang Z, Wang F, Zhu G, Zhang X (2011) Simulation of tube forming process in Mannesmann mill. J Shanghai Jiaotong Univ (Sci) 16(3):281–285. https://doi.org/10.1007/s12204-011-1144-1
47. Pater Z, Kazanecki J (2013) Complex numerical analysis of the tube forming process using Diescher mill. Arch Metall Mater 58(3):717–724. https://doi.org/10.2478/amm-2013-0060
48. Pater Z, Tomczak J, Bartnicki J, Lovell MR, Menezes PL (2013) Experimental and numerical analysis of helical-wedge rolling process for producing steel balls. Int J Mach Tool Manu 67:1–7. https://doi.org/10.1016/j.ijmachtools.2012.12.006
49. Tomczak J, Pater Z, Bulzak T (2014) Designing of screw impressions in helical rolling of balls. Arch Civ Mech Eng 14:104–113. https://doi.org/10.1016/j.acme.2013.07.004
50. Cao Q, Hua L, Qian D (2015) Finite element analysis of deformation characteristics in cold helical rolling of bearing steel-balls. J Cent South Univ 22:1175–1183. https://doi.org/10.1007/s11771-015-2631-6
51. Pater Z, Tomczak J, Bulzak T (2015) Numerical analysis of the skew rolling process for rail axles. Arch Metall Mater 60:415–418. https://doi.org/10.1515/amm-2015-0068
52. Xu C, Shu X (2018) Influence of process parameters on the forming mechanics parameters of the three-roll skew rolling forming of the railway hollow shaft with 1: 5. Metalurgija 3:153–156
53. Li Z, Shu X (2019) Involute curve roller trace design and optimization in multipass conventional spinning based on the forming clearance compensation. ASME J Manuf Sci Eng 141(9):091007. https://doi.org/10.1115/1.4044007
54. Berti GA, Quagliato L, Monti M (August 2015) Set-up of radial–axial ring-rolling process: process worksheet and ring geometry expansion prediction. Int J Mech Sci 99:58–71. https://doi.org/10.1016/j.ijmecsci.2015.05.004
55. Quagliato L, Berti GA. Mathematical definition of the 3D strain field of the ring in the radial-axial ring rolling process. Int J Mech Sci, September 2016;115–116;746–759. https://doi.org/10.1016/j.ijmecsci.2016.07.009
56. Groche P, Kramer P (2018) Numerical investigation of the influence of frictional conditions in thread rolling operations with flat dies. Int J Mater Form 11:687–703. https://doi.org/10.1007/s12289-017-1383-2
57. Quagliato L, Berti GA, Kim D, Kim N (2018) Contact geometry estimation and precise radial force prediction for the radial-axial ring rolling process. Int J Mater Form 11:789–805. https://doi.org/10.1007/s12289-017-1388-x